Journal of Power Sources 625 (2025) 235625

Contents lists available at ScienceDirect

Journal of Power Sources

journal homepage: www.elsevier.com/locate/jpowsour

Cobalt oxide (CoO_x) coated Ni foam anodes for high temperature (150 °C) and pressure (45 bar) alkaline electrolysis

Pradipkumar Leuaa [a,*], Yousef Alizad Farzin [a,b], Sarmad Iqbal [a], Christodoulos Chatzichristodoulou [a,**]

[a] Department of Energy Conversion and Storage, Technical University of Denmark (DTU), 2800, Kongens Lyngby, Denmark
[b] Institute for Applied Materials - Electrochemical Technologies (IAM-ET), Karlsruhe Institute of Technology (KIT), Adenauerring 20b, 76131, Karlsruhe, Germany

HIGHLIGHTS

- Ni foam (NF), CoOx/NF and Inconel/NF electrodes are assessed as anodes for HTP-AE.
- Increasing operating temperature reduces the overpotential of the anode.
- Low current densities (10–100 mA/cm^2) are inadequate to assess electrode stability.
- The CoO_x/NF electrode showed remarkable activity and stability at 150 °C, 45 bar.

ARTICLE INFO

Keywords:
Alkaline electrolysis
Cobalt oxide
High temperature and pressure electrochemistry
Inconel
Oxygen evolution reaction

ABSTRACT

CoO_x-coated Ni foam (CoO_x/NF) electrodes are evaluated as anodes for high temperature and pressure (HTP) alkaline electrolysis. The electrodes are tested for the oxygen evolution reaction (OER) from room temperature to 150 °C at 45 bar pressure in 45 wt% KOH and compared with commercially available pristine NF and Inconel-coated NF (Inconel/NF) electrodes. Although the Inconel/NF electrode shows the best performance at 25 °C and 45 bar pressure, the performance of CoO_x/NF and Inconel/NF become comparable upon raising the operating temperature to 150 °C. During a long-term (108 h) stability test at 150 °C and 45 bar pressure, the CoO_x/NF electrode maintained stable performance, requiring an overpotential of 185 mV at 500 mA cm^{-2}. In contrast, the Inconel/NF electrode experienced an increase in overpotential from 182 mV to 208 mV after 84 h of operation under identical conditions. The structural and chemical changes in these electrodes were investigated using post-mortem scanning electron microscopy (SEM) and X-ray photoelectron spectroscopy (XPS), comparing their evolution to that of the fresh electrodes.

1. Introduction

Electrolytic hydrogen production plays a crucial role in moving towards sustainable energy systems, as it allows for the creation of eco-friendly chemicals and fuels using renewable electricity sources. Among the primary electrolysis technologies, alkaline electrolysis (AE) stands out as the most suitable for the needed hundreds of gigawatts of capacity. This is due to its reliance on low-cost, abundant materials and its proven track record of scalability [1–4]. However, AE has limitations in terms of efficiency and productivity. Enhancing operating temperature and pressure can help mitigate these shortcomings [5–8]. For instance, an AE cell operating at 200 °C and 20 bar achieved a record high current density of 3.75 A cm^{-2} at 1.75 V, corresponding to an 85 % electrical efficiency [9]. This represents roughly a tenfold increase in productivity compared to state-of-the-art AE cells functioning at 80–100 °C. To develop these innovative concepts into practical technological devices, further research into electrode materials and designs is essential, as electrodes are critical in determining the overall performance of electrochemical systems [10–13]. Developing electrodes that maintain high performance and stability in the corrosive alkaline environment at HTP is particularly challenging, especially for the O_2-evolving anode.

* Corresponding author.
** Corresponding author.
E-mail addresses: pmale@dtu.dk, pradeepleuaa@gmail.com (P. Leuaa).

https://doi.org/10.1016/j.jpowsour.2024.235625
Received 4 July 2024; Received in revised form 9 October 2024; Accepted 14 October 2024
Available online 25 October 2024

Catalyst and electrode stability are often neglected or insufficiently investigated, with most of the reported electrodes only tested under ambient temperature and pressure in dilute electrolyte solutions (0.1–1 M KOH), far from the typical operating conditions of industrial AE; 70–90 °C, 25–35 wt% KOH, 1–30 bar. These harsh conditions can cause structural changes and degradation in the electrodes. The electrode degradation is mostly due to catalyst agglomeration, modification, dissolution, and/or detachment from the substrate [14]. Modification and dissolution depend on the stability of the catalyst material under operating conditions, and the possible formation of protective passivation layers. To prevent agglomeration and detachment, it is crucial to ensure a stable connection between the support and the catalyst.

Nickel is commonly employed as an electrode support material in conventional AE due to its corrosion resistance in alkaline environments. Additionally, nickel oxyhydroxide exhibits strong electrochemical performance for the OER, which significantly enhances upon incorporation of iron [15–17]. Earlier work by Schmitz et al. on highly porous nickel anodes showed slow degradation over 7200 h at 100 °C when operated in a dynamic mode, reverting between 10 h at 400 mA cm^{-2} and 14 h at open circuit potential [18,19]. Prigent et al. reported that Ni electrodes are unstable at temperatures above 160 °C due to excessive oxidation [20,21]. Currently, NiFe-based oxyhydroxides are the most active electrocatalysts reported for the OER in alkaline media up to 80 °C. However, at elevated temperatures, Fe tends to leach out from the NiFe catalyst [22] which may challenge the implementation of NiFe-based catalysts at HTP and even conventional technological AE conditions. Other than NiFe, CoO_x-deposited Ni electrodes are well-known stable OER catalysts [23–26]. Cobalt is known to form stable oxides, such as CoO and Co_3O_4 [27,28], which are resistant to further oxidation and dissolution. These oxides adhere well to the Co surface, forming a protective layer that prevents degradation of the underlying material. Moreover, the Pourbaix diagrams of cobalt and iron in alkaline media shows that cobalt has a broader region of stability for its oxides, particularly Co_3O_4, at higher pH values [29]. This stability region prevents cobalt from dissolving or undergoing rapid oxidation under typical alkaline conditions. Wendt et al. tested four different types of anodes, such as bare Ni and $La_{0.5}Sr_{0.5}CoO_3$-, $NiCo_2O_4$- and Co_3O_4--coated perforated Ni plates in the temperature range of 50–130 °C. The $La_{0.5}Sr_{0.5}CoO_3$ perovskite-coated Ni electrode exhibited good activity, but after 200 h of operation at 1 A cm^{-2} and 90 °C, Sr was completely leached out [30,31]. Co_3O_4 spinel-coated Ni electrodes exhibited the highest activity, requiring an overpotential of 290 mV at 1 A cm^{-2} when operated at 90 °C. However, they observed fast degradation for all Co-activated anodes for overpotentials exceeding 270 mV [30,31], leaving open the question of the CoO_x catalyst stability at lower overpotentials in HTP conditions.

Moreover, Wendt et al. reported the effect of the pore size of the Ni substrate on the performance and concluded that small pore sizes tend to trap oxygen bubbles and lead to increased cell voltage [31]. In our recent study, involving six distinct types of Ni substrates spanning from 2D Ni mesh and perforated plates to 3D Ni foams of different pore sizes, we demonstrated that 3D Ni foams with large pores combine increased surface area with efficient gas release [13]. Consequently, we opted for NF substrates in the present work and report the preparation of CoO_x--coated Ni foam (CoO_x/NF) electrodes and investigated their electrochemical performance and stability for the OER at HTP-AE conditions.

For comparison, commercially available Inconel-coated NF electrodes were also tested at HTP conditions, anticipating the in-situ formation of NiFe-based oxyhydroxide at the surface of the starting nickel-chromium-based superalloy that also contains approx. 5 % iron, in line with previous corrosion engineering attempts [32,33]. This approach is very promising in terms of reducing electrode cost while boosting performance. Continuous corrosion of the starting Inconel alloy is nevertheless a concern when applying the corrosion engineering approach. Inconel alloy comprises approximately 22 % Cr and 10 % Mo, both of which may remain to some extent in the developing NiFe-based oxyhydroxide and oxides, influencing the electrochemical activity for the OER. Doping Mo into transition metal oxides modifies the electronic structure and associated density of states, which enhances the binding energy of oxygen intermediates and reduces the OER overpotential [34,35]. Mo-doped Nickel-Iron Oxides ($NiFeMoO_x$) are extensively studied electrocatalysts for OER [36,37]. Similarly, Chromium (Cr) is frequently used as a dopant in transition metal oxides [38–41] and reported to generate defects or oxygen vacancies which can serve as catalytic active sites. Rosalbino et al. investigated the electrocatalytic activity of a crystalline (Ni-Co-Cr)-based alloy for the OER and reported that Cr exhibits a higher enthalpy of OH* adsorption for the OER compared with Ni which enhances the catalytic activity of the electrode towards the OER [42,43]. Given the extensive research on Ni, Fe, Cr and Mo-based catalysts for OER, a long-term stability study was also undertaken for the Inconel/NF electrodes at HTP conditions.

2. Experimental

2.1. Materials

KOH (ACS reagent., >85 % KOH basis, pellets, Fluka) was obtained from Sigma Aldrich. Nickel foam (NF) and Inconel-coated NF electrodes were procured from Alantum Corporation. Co_3O_4 nanopowder (99 %, Metals Basis) with a mean particle size of 50–80 nm was procured from Alfa Aesar.

2.2. CoO_x/NF electrode preparation

A slurry was prepared by mixing cobalt oxide and binders in a ratio of 20:80 wt% (Co_3O_4: binder) and roll-mill the mixture at a speed of 45–60 rpm for 24 h. The binder contained 12 wt% Polyvinylpolypyrrolidone (PVP) K15, 6 wt% PVP K90, and 82 wt% ethanol. Cylindrical balls with a diameter of 9.6 mm were used for roll-milling, and the balls-to-powder weight ratio was 10. For the coating step, the NF was compressed mechanically by a hydraulic press to the thickness of 450 μm. For cleaning the substrate, the NF was sonicated in 5.0 M HCl solution and subsequently in ethanol for 15 min, and then it was washed thoroughly with deionized water. The NFs (4 × 4 cm^2) were dip-coated with the Co_3O_4 slurry at the dipping and withdrawal speed of 0.1 cm/s. Afterwards, the substrates were hung for drying overnight under ambient conditions. Then, the samples were sintered at 500 °C for 1 h in the oxidizing-reducing atmosphere with a heating and cooling ramp rate of 30 °C/h. During the initial heating procedure, the air was utilized to burn out the organic component, switching to N_2 and then 5 vol% H_2/N_2 at the target temperature for reductive sintering.

2.3. Electrochemical characterization

All electrochemical measurements were performed in 45 wt% KOH solution prepared from KOH pellets and 18.2 MΩ cm^2 (Milli-DI®) water. The KOH solution was pre-electrolyzed with nickel electrodes at 2.0 V for 24 h before being used to suppress impurities. All electrochemical testing was conducted using a SP−300 potentiostat from BioLogic Science Instruments (Seyssinet-Pariset, France). A Parr autoclave Type 4760, featuring a 600 ml volume and a PTFE (Polytetrafluoroethylene) liner, was utilized for the HTP electrochemical measurements. The autoclave included additional gas handling components and wire throughputs, and it was pressurized using N_2. A more detailed description can be found in a prior publication [44]. A custom-made PEEK cell was used with a previously developed ceramic separator (see Fig. S1 in the supplementary information (SI)) [7]. The as-prepared CoO_x/NF electrode (2.5 × 2.5 cm^2) was used as a working electrode, and to avoid contamination from the cathode, pristine NF was used as a counter electrode, whereas an in-house made reversible hydrogen electrode (RHE) was used as a reference electrode. The details of the preparation method for the stable RHE in HTP conditions are described in our

previous work [45]. All the polarization curves were recorded stepwise at selected current densities and at each step, the current was held for 60 s whereas the potential was measured as an average of the last 30 s. The galvanostatic electrochemical impedance spectra (GEIS) were recorded in the frequency range of 10 KHz to 100 mHz with an ac amplitude of 5 % of the applied DC current. The impedance spectra were fitted using the CNLS method with "ZSimpWin" software from Solartron and the solution resistance (R_s) obtained from the GEIS recorded at 10 mA cm^{-2} was used for iR-correction.

2.4. Microstructural and chemical characterization

The microstructure of the pristine and tested NF, CoO_x/NF, and Inconel/NF electrodes was studied with a field emission scanning electron microscope (FE-SEM, Zeiss-Merlin), and the near-surface chemical composition was investigated by X-ray photoelectron spectroscopy (Escalab 250 Xi-XPS). X-ray diffraction (XRD) spectra were obtained with an Aeris powder diffractometer (Cu Kα radiation, λ = 1.5406 Å).

3. Results and discussion

3.1. Physical-chemical evaluation

XRD patterns of pristine NF, as prepared CoO_x/NF, and electrochemically conditioned CoO_x/NF electrode are shown in Fig. 1. The pristine NF electrode shows three major peaks at approximately 44.5, 51.9, and 76.4° (2θ), corresponding to the metallic Nickel phase [46]. The as-prepared CoO_x/NF electrode reduced sintered at 500 °C in 5 vol% H_2/N_2, shows a similar XRD pattern (Fig. 1(b)) due to the formation of a metallic Co phase [47]. Since metallic Co and Ni have similar peak positions in XRD, distinguishing between them becomes challenging. The as-prepared CoO_x/NF electrode is labeled as Co/NF from hereon to indicate that the initial phase of the coating on the reduced sintered electrode is metallic Co. Further, the Co/NF electrode was conditioned electrochemically (detailed procedure in SI) and the XRD pattern of this conditioned electrode shows additional weak peaks corresponding to the Co_3O_4 and CoO phases (see Fig. 1(c)) [46,47]. Therefore, the electrochemically conditioned electrodes are labeled as CoO_x/NF throughout the manuscript.

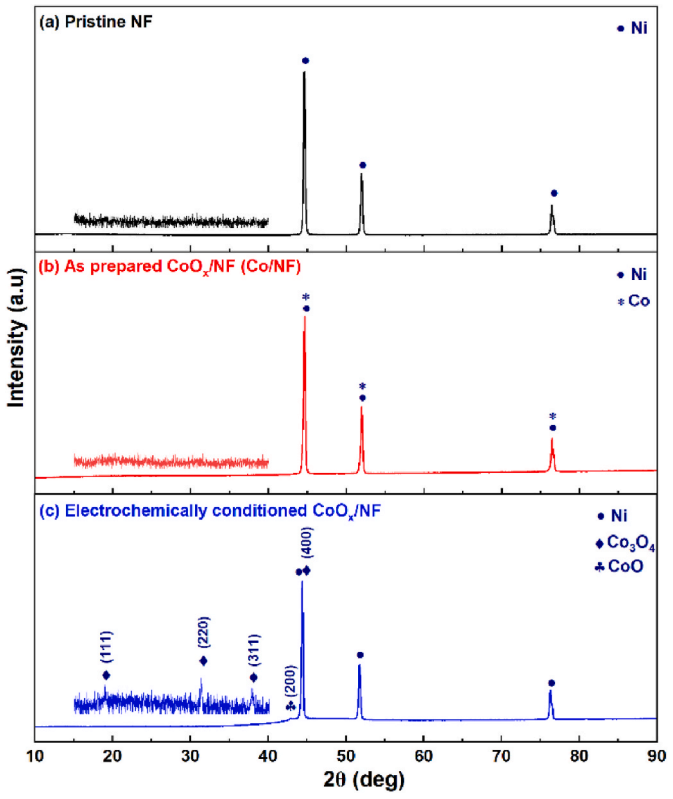

Figure 1. XRD patterns of (a) pristine NF, (b) as prepared Co/NF, and (c) electrochemically conditioned CoO_x/NF electrode.

The morphology of pristine NF, as prepared Co/NF, and Inconel/NF electrodes was investigated by SEM (Fig. 2). The pristine NF is highly porous (>92 %) with an estimated pore size in the range of 180 ± 50 μm. At low magnification, the surface of pristine NF appears smooth, whereas the as-prepared Co/NF sample displays an uneven catalyst coating (Fig. 2(b)), with higher accumulation in the concave parts of the foam structures. In the high-magnification SEM images, the Co coating appears porous, exhibiting a distribution of macropores. During the electrochemical conditioning, the phase transition from metallic Co to CoO_x significantly modifies the structure, causing the macropore-like structure to reorganize into a flake-like structure, as shown in Fig. 2 (c). The Inconel/NF samples exhibit a layer of well-connected particulate Inconel covering the surface of the NF (Fig. 2(d)).

3.2. Electrochemical performance at room temperature

For the electrochemical testing, electrodes were placed in the electrochemical cell (see Fig. S1) filled with 45 wt% KOH and conditioned by keeping them at 10 mA cm^{-2} for at least 1 h or until a stable potential was observed (see the corresponding chronopotentiometry graph in SI). Once the electrodes were conditioned, the electrochemical cell was placed in the autoclave, and the pressure was increased to 45 bar. The CV response of NF, CoO_x/NF, and Inconel/NF electrodes at 25 °C and 45 bar is shown in Fig. 3(a). The CV of the pristine NF electrode shows a prominent oxidation peak at ~1.45 V and a corresponding reduction peak at ~1.2 V, which are attributed to the conversion between $Ni(OH)_2$ and NiOOH [16]. The $Ni(OH)_2$ oxidation peak appeared suppressed in CoO_x/NF, and two distinct oxidation peaks were observed. The first peak at ~1.05 V corresponds to Co_3O_4 oxidation to CoOOH, whereas the second peak at ~1.3 V corresponds to further oxidation to CoO_2 according to the following reactions [48,49]:

$$Co_3O_4 + OH^- + H_2O \rightarrow 3CoOOH + e^- \quad (1)$$

$$CoOOH + OH^- \rightarrow CoO_2 + H_2O + e^- \quad (2)$$

The OER overpotential of the NF electrode is ~445 mV at 10 mA cm^{-2}, whereas for the CoO_x/NF electrode, it reduces to ~258 mV. For the Inconel/NF electrode, the Ni oxidation peak is pronounced and appears to be merged with the OER, which is shifted to lower potentials compared to the pristine NF. The Inconel/NF electrode requires an OER overpotential of ~209 mV at 10 mA cm^{-2}, showing better performance than CoO_x/NF. The steady-state response of these electrodes is compared in Fig. 3(b), with both CoO_x/NF and Inconel/NF showing much better performance compared to the pristine NF.

3.3. Effect of temperature

The electrode performance was then determined while increasing the temperature from 25 to 150 °C in steps of 25 °C. Fig. 4(a) shows the GEIS of CoO_x/NF recorded at 10 mA cm^{-2} at each temperature step. The impedance spectra were fitted with the Randles equivalent circuit as shown in the inset of Fig. 4(a), where R_s is the solution resistance, R_{ct} is the charge-transfer resistance, and C is the associated capacitance. The R_s and R_{ct} values with temperature are shown in Fig. 4(b). The R_s decreases with increasing temperature due to the thermally activated electrolyte conductivity [7]. The R_{ct} also decreases with increasing temperature, indicating increased OER reaction kinetics. A similar trend is observed in the impedance spectra of the NF and Inconel/NF electrodes (see Fig. S3 in SI).

Activation energies were obtained from Arrhenius plots, as shown in

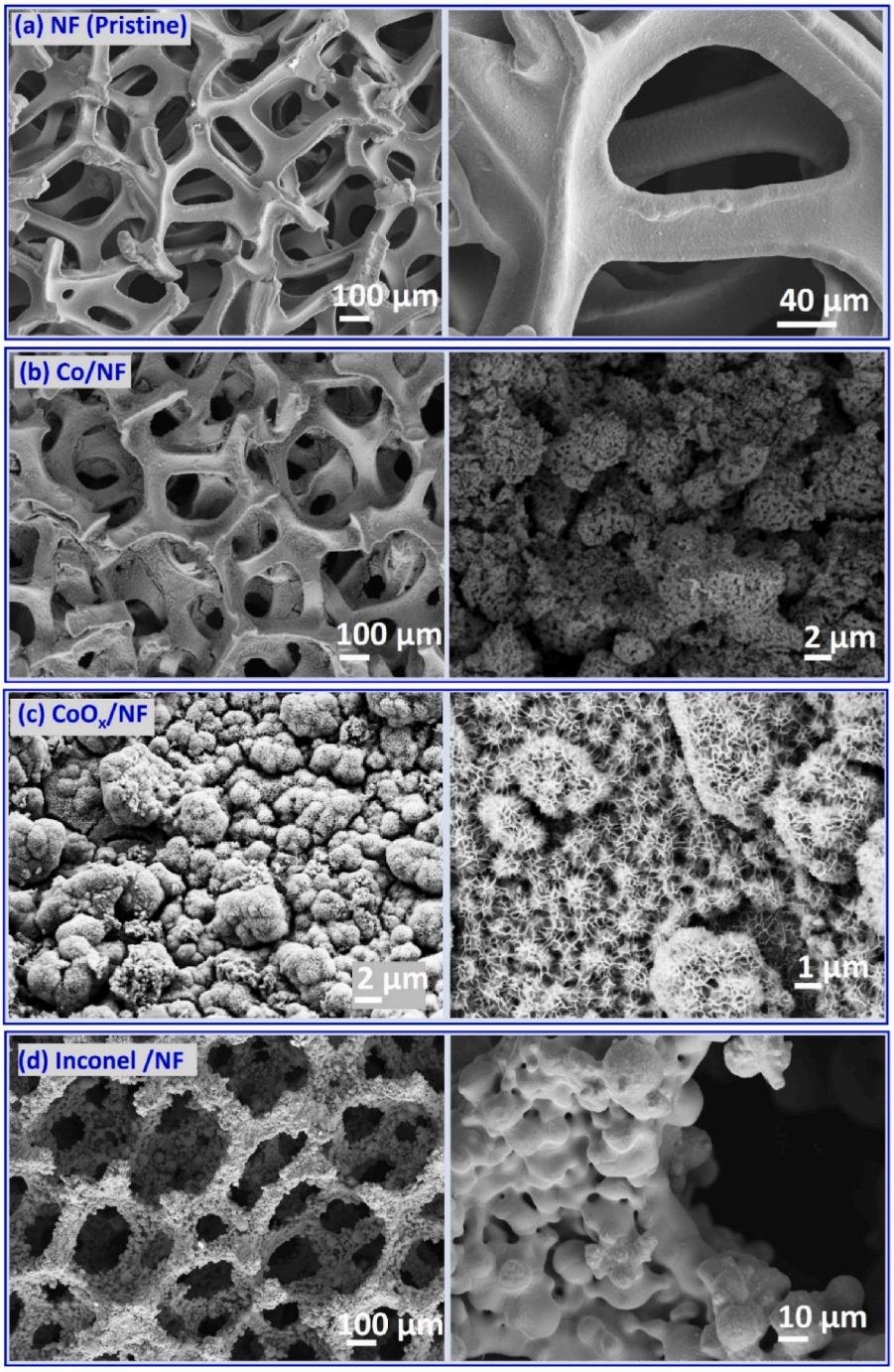

Fig. 2. SEM images of (a) pristine NF, (b) as prepared Co/NF (c) electrochemically conditioned CoO_x/NF and (d) Inconel/NF electrodes at various magnifications.

Fig. 4(c). The Inconel/NF electrode shows the least activation energy of 0.0154 eV, whereas NF and CoO_x/NF electrodes show 0.067 and 0.039 eV, respectively. Fig. 4(e) shows the steady-state polarization curves of the CoO_x/NF electrode with the increase in temperature. The performance of the electrode shows a very pronounced thermal activation with the electrode overpotential at 500 mA cm^{-2} decreasing from 0.394 V at 25 °C to 0.186 V at 150 °C, corresponding to a decrease of 1.66 mV/K. The electrode overpotential was derived from the measured electrode potential versus $RHE^{T/P}$ after adjusting for the change in the Gibbs free energy for water splitting with temperature and pressure [45,50] as described in the SI. In line with the determined activation energies, more pronounced thermal activation was observed for the pristine NF, its overpotential at 500 mA cm^{-2} decreasing from 0.719 V at 25 °C to 0.295 V at 150 °C, corresponding to a decrease of 3.39 mV/K (Fig. 4(d)). The Inconel/NF electrode, on the other hand, showed the smallest thermal activation, its overpotential at 500 mA cm^{-2} decreasing from 0.299 V at 25 °C to 0.181 V at 150 °C, corresponding to a decrease of 0.94 mV/K (Fig. 4(f)). An inverse correlation was observed between performance and thermal activation, with CoO_x/NF and Inconel/NF yielding similar performance at 150 °C and even bare NF requiring only ~110 mV higher overpotential at 500 mA cm^{-2} at 150 °C.

The Tafel slope was estimated in two different current density regions of the steady-state iV curves recorded on all three electrodes with an increase in temperature and summarized in Table S2 in SI. In the low current density region (10–100 mA cm^{-2}), the Inconel/NF sample shows the lowest Tafel slope of 44 mV.dec^{-1} at 25 °C, which increases

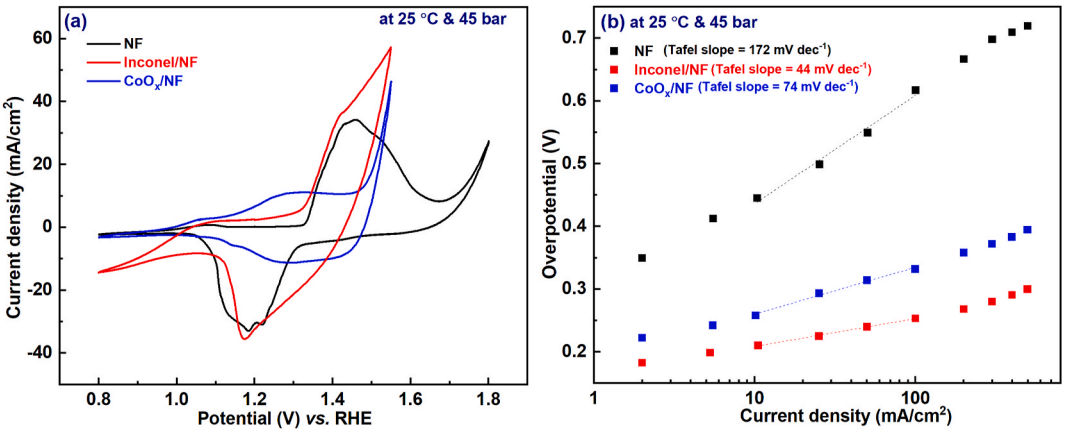

Fig. 3. (a) Cyclic voltammetry and (b) Tafel plots of NF, Inconel/NF, and CoO_x/NF electrodes recorded in 45 wt % KOH at 25 °C and 45 bar pressure.

marginally to 51 mV.dec^{-1} at 150 °C. Conversely, for the CoO_x/NF sample, the Tafel slope decreased from 74 mV.dec^{-1} to 59 mV.dec^{-1} with the increase in temperature from 25 °C to 150 °C. These relatively small Tafel slope values are typical for good catalysts and reflect a varying concentration of reaction intermediates with overpotential. For the pristine NF sample, a prominent effect of temperature was observed, reducing the Tafel slope from 172 mV.dec^{-1} at 25 °C to 78 mV.dec^{-1} at 150 °C. In the high current density region (200–500 mA cm^{-2}), the Tafel slope increased with temperature for all three electrodes, and at 150 °C, it was found to be quite similar for CoO_x/NF (124 mV.dec^{-1}) and Inconel/NF (121 mV.dec^{-1}) samples. The increase in Tafel slope at higher current density region reflects the combined effect of a gradual stabilization of reaction intermediate concentrations, as well as mass transport contributions that can be significant when testing in a zero-gap configuration without imposed electrolyte flow.

3.4. Stability test at 150 °C and 45 bar pressure

The long-term stability of the electrodes at 150 °C and 45 bar was evaluated in two stages, starting with a mild operating profile, subjecting them to a current density of 10 mA cm^{-2} for 24 h, as shown in Fig. 5(a). Throughout this period, GEIS was conducted at 4-h intervals. All three electrodes showed a stable overpotential over the 24-h duration at 10 mA cm^{-2}. Moreover, the R_{ct} obtained from the EC fitting of the impedance data was observed to be stable for all three electrodes. To further probe their stability under more aggressive conditions, chronopotentiometry (CP) measurements were conducted at elevated and varying current densities, sequentially cycling the current density from 10 mA cm^{-2} for 90 min to 100 mA cm^{-2} for 20 min, then 250 mA cm^{-2} for 10 min, and finally 500 mA cm^{-2} for 5 min. These CP cycles were repeated on the NF electrode for more than 72 h, as shown in Fig. 5(b). The pristine NF electrode appears to maintain stable overpotential even after prolonged operation at high current densities. At 10 mA cm^{-2}, the electrode potential fluctuates within ±1 mV, which gradually increases with increasing current density, reaching ±5 mV at 500 mA cm^{-2}. This is likely associated with the dynamic nucleation-growth/coalescence-release of bubbles from the electrode surface. The stability of the CoO_x/NF and Inconel/NF electrodes were tested similarly, as shown in Fig. 5(c) and (d), respectively. The CoO_x/NF electrode appears to maintain a stable overpotential for more than 108 h of operation at high current densities. The Inconel/NF electrode exhibited relatively stable performance during the initial 24 h (10 cycles). However, a gradual degradation was observed after that, resulting in an overpotential increase of ~26 mV at 500 mA cm^{-2} after 84 h of continuous cycling. These findings suggest that commonly employed low current densities, 10–100 mA cm^{-2}, and low operating temperatures are insufficient for assessing electrode stability.

During these CP cycling measurements, GEIS were systematically recorded at each CP step. Fig. 5(e) and (f) present the EIS recorded initially and after the final CP cycle at 500 mA cm^{-2} for the CoO_x/NF and Inconel/NF electrodes, respectively. Notably, the impedance spectra for the CoO_x/NF electrode overlap even after 108 h of CP cycling. In contrast, the Inconel/NF electrode manifests an increased semi-circle diameter, indicating elevated charge-transfer resistance. The EIS spectra recorded at every 12 h of CP cycling were fitted with EC, and the corresponding R_{ct} are shown in Fig. 5(g). For the NF and CoO_x/NF electrode, the R_{ct} was found to remain constant throughout the CP cycling test. Conversely, for the Inconel/NF electrode, the R_{ct} showed a steady increase after 24 h, aligning with the observed overpotential increase. By the end of each test, the KOH volume decreased from an initial 30 mL to 25 mL. Despite the rise in KOH concentration from 11.6 M to approximately 14.0 M, the R_s remained stable throughout the entire test period for all three samples (see Fig. S4 in SI).

3.5. Post-mortem analysis of electrodes

At the end of the long-term stability test, the autoclave was cooled down to 25 °C while maintaining 45 bar pressure inside. At these conditions, the i-V curves of the electrodes were recorded to compare with their initial performance at 25 °C and 45 bar, as shown in Fig. S5 in SI. The NF electrode showed significant improvement in performance at the end of the test at 25 °C and 45 bar. Similarly, the CoO_x/NF electrode showed a marginal improvement, likely due to the increased surface area following the electrochemical test at HTP. In contrast, the Inconel/NF electrode showed a slightly degraded performance, consistent with the degradation observed during the long-term electrochemical test under HTP conditions.

The microstructural changes of all electrodes after electrochemical testing were examined using SEM, as illustrated in Fig. 6. The pristine NF electrode appears roughened after electrochemical testing, with the development of a porous layer (Fig. 6(a')). The phase composition of this layer was analyzed by XRD, revealing the presence of NiO, NiOOH, and Ni_2O_3 phases (Fig. S13 in SI). Fig. 6(b) displays SEM images of the CoO_x/NF electrode, showing nanoflake-like structures within the unevenly distributed macropores of CoO_x particles on the NF surface. The post-mortem images of the electrochemically tested CoO_x/NF electrode show a somewhat modified microstructure with uniformly distributed nanoflakes across the NF surface (Fig. 6(b')). Energy dispersive spectroscopy (EDS) revealed the presence of Co in these nanoflake structures (see results of EDS mapping in SI). This post-mortem analysis suggests that the CoO_x coating recrystallizes during operation but remains dynamically stable even after prolonged exposure to elevated temperature and pressure and at high current densities. XRD analysis of the CoO_x/NF electrode reveals a mixed-phase composition of CoOOH, CoO,

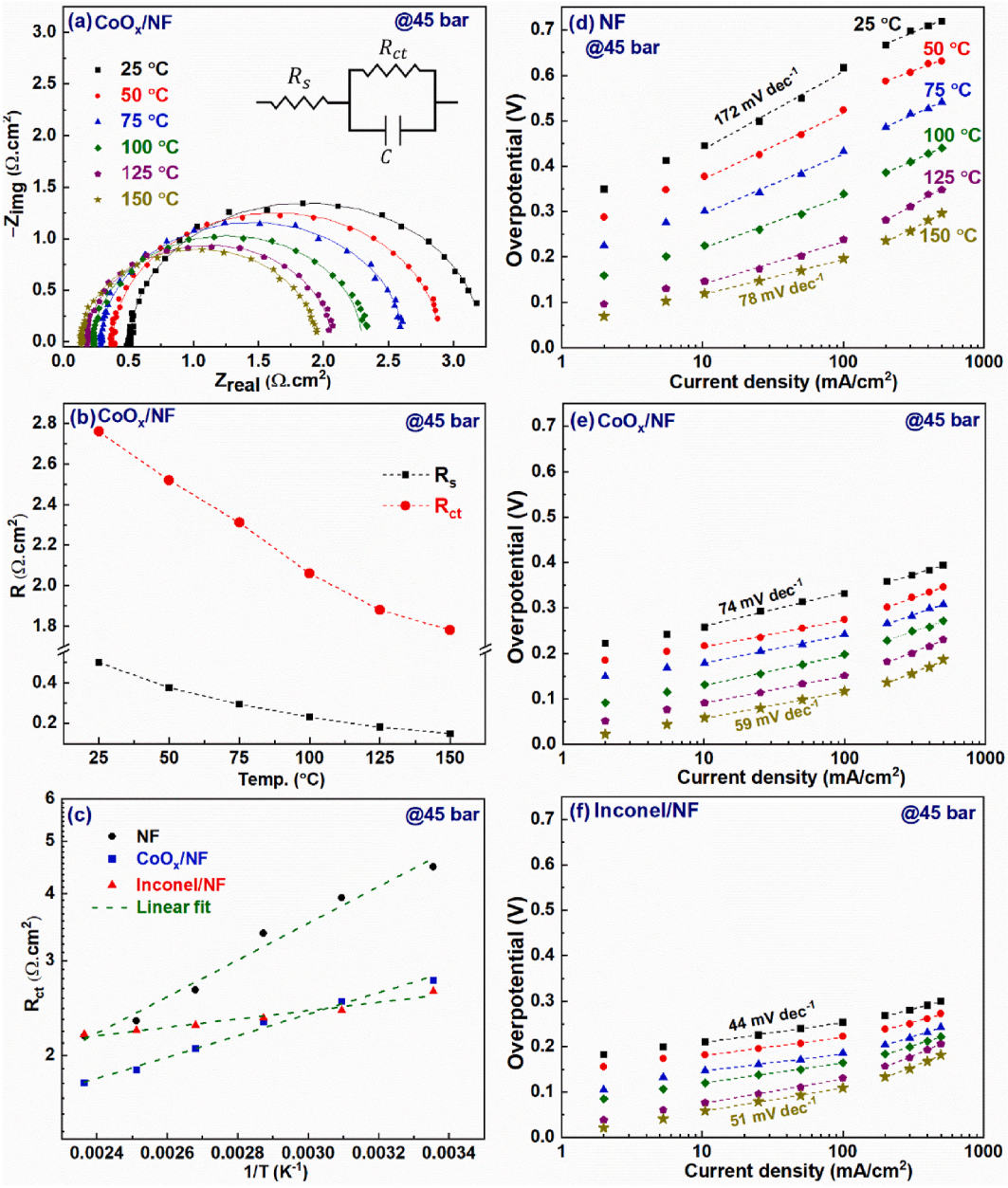

Figure 4. (a) GEIS of CoO_x/NF electrode recorded at 10 mA cm^{-2} upon increasing temperature, (b) solution resistance (R_s) and charge-transfer resistance (R_{ct}) obtained from EC fitting of EIS and (c) corresponding Arrhenius plot, and (d), (e) and (f) Tafel plots of pristine NF, CoO_x/NF and Inconel/NF electrodes, respectively.

and Co_3O_4, with possible Ni incorporation in all of these phases. However, unlike the NF electrode, the Ni_2O_3 phase was not observed, likely because of the lower overpotentials required in the presence of the CoO_x coating (Fig. S13 in SI). The XRD analysis was inconclusive concerning the formation of NiO due to the coincidence of its diffraction pattern with that of CoO.

Fig. 6(c) shows top and cross-sectional view (CSV) SEM images of the pristine Inconel/NF electrode. As discussed in Fig. 1, large (5–50 μm), dense, spherical Inconel particles with smooth surfaces cover the NF surface. After prolonged electrochemical testing at 150 °C and 45 bar, the particles exhibit surface corrosion, forming a porous shell (Fig. 6 (c')). The EDS mapping suggests that Mo, Si, Nb, and Cr are the elements that leached out from the surface of the Inconel particles (see results of EDS mapping in SI). Initially, the weight ratios of Mo/Ni, Cr/Ni, Si/Ni, and Nb/Ni were 0.436, 0.33, 0.08, and 0.188, respectively. After testing, these ratios changed to 0.008, 0.163, 0.00, and 0.01, respectively, indicating complete leaching of Mo, Si, and Nb and partial removal of Cr, likely causing the degradation in electrochemical performance despite the increased surface area.

XPS measurements were also performed to investigate the surface composition and chemical state of the prepared and electrochemically tested electrodes. The XPS survey spectra of the as-prepared and electrochemically tested CoO_x/NF electrodes reveal signals from Ni, Co, and O (Fig. S14). The core level Co 2p spectra of the as-prepared and tested CoO_x/NF samples are shown in Fig. 7(a) and (a'), respectively. The spectra display two peaks corresponding to the $2p_{3/2}$ and $2p_{1/2}$, followed by satellites [51–53]. The XPS spectra were decomposed using Voigt peak fitting functions within the Shirley background, and the fitting parameters and results of the quantitative analysis are summarized in Table S7 in SI. Constrained peaks with equal full width at half maximum (FWHM) and constant area ratio of $(2p_{3/2})/(2p_{1/2})$ according to the number of electrons in the p orbitals were used to fit the Co 2p and Ni 2p spectra [54,55].

Adopting a constant area ratio of 2 for the $2p_{3/2}/2p_{1/2}$ in the Co 2p

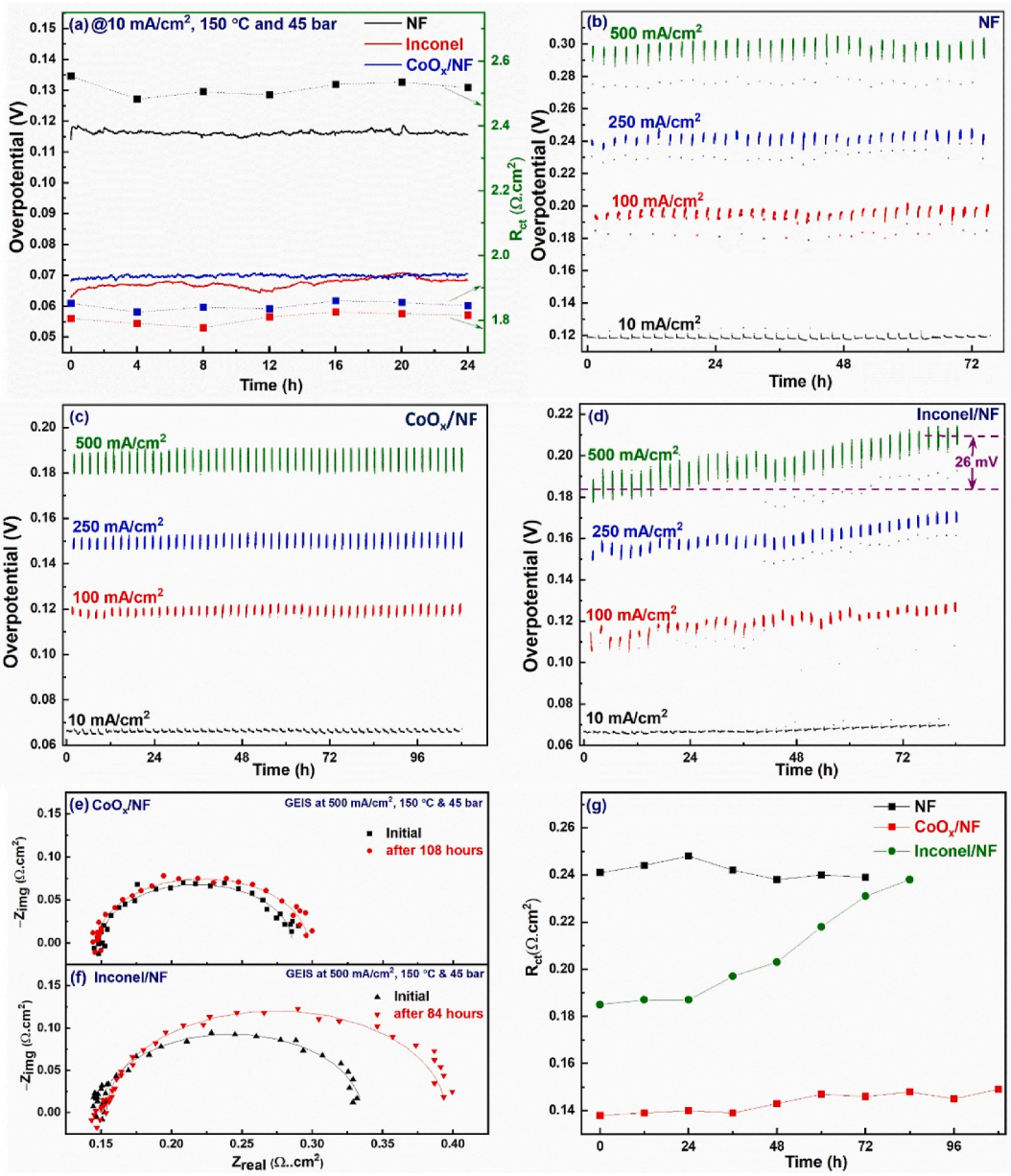

Figure 5. (a) Overpotential of NF, CoO_x/NF, and Inconel/NF electrodes at 10 mA cm^{-2} for 24 h at 150 °C and 45 bar along with the R_{ct} obtained from GEIS fitting, CP measurements of (b) NF (c) CoO_x/NF and (d) Inconel/NF electrodes upon cycling current density between 10, 100, 250, and 500 mA cm^{-2} at 150 °C and 45 bar, GEIS of (e) CoO_x/NF and (f) Inconel/NF electrode at 500 mA cm^{-2} and, (g) R_{ct} obtained from EC fitting of the GEIS.

spectra is incompatible with the experimental data. Following Biesinger et al. [56], we attribute this to the formation of metallic Co in the as-prepared electrode, represented by an additional peak at a binding energy of 778.2 eV with FWHM = 0.81 in the fitting of the Co $2p_{3/2}$ orbital. The fitting parameters for the Co^0, Co^{2+}, and Co^{3+} are compatible with previous reports for metallic Co and Co oxides [56,57]. The quantitative analysis showed 17.4 at.% Co^0 after reductive sintering, and 22.1 and 60.5 at.% of Co^{2+} and Co^{3+}, respectively. After testing the electrode, the fitted peaks reveal oxidation of Co^0, which results in increasing Co^{2+} and Co^{3+} concentrations to 32.1 and 67.9 at.%, respectively (Fig. 7(a')).

The core level Ni 2p spectrum of the as-prepared CoO_x/NF sample is shown in Fig. 7(b). The spectrum displays peaks at binding energies of 852.7 and 869.8 eV, which correspond to metallic Ni, and peaks at binding energies of 854.3 and 871.7 eV, which correspond to Ni^{2+} from surface oxidation of Ni upon air exposure [51,58]. The Ni 2p spectrum for the tested CoO_x/NF sample reveals additional peaks at the binding energy of 856.3 and 873.9 eV corresponding to Ni^{3+} ions, likely due to superficial oxidation of NiO to NiOOH and Ni_2O_3 and/or incorporation of Ni in CoOOH and the Co_3O_4 spinel (Fig. 7(b')). Similarly, for the NF sample, peaks corresponding to Ni^{3+} ions were observed in the post-mortem XPS (Fig. S15 in SI).

The XPS survey spectra of pristine and electrochemically tested Inconel/NF electrodes are shown in Fig. 8. The elements observed in detectable quantities on both sample surfaces were Ni, Cu, Co, Fe, Mn, C, and Al [59]. However, peaks corresponding to Cr, Mo, and Nb are observed only on the surface of the pristine Inconel/NF sample, showing that these elements leach out during electrochemical testing, likely associated with the observed degradation.

4. Conclusions

Pristine NF, CoO_x-coated NF, and Inconel-coated NF electrodes were assessed as anodes for HTP alkaline electrolysis. The electrodes

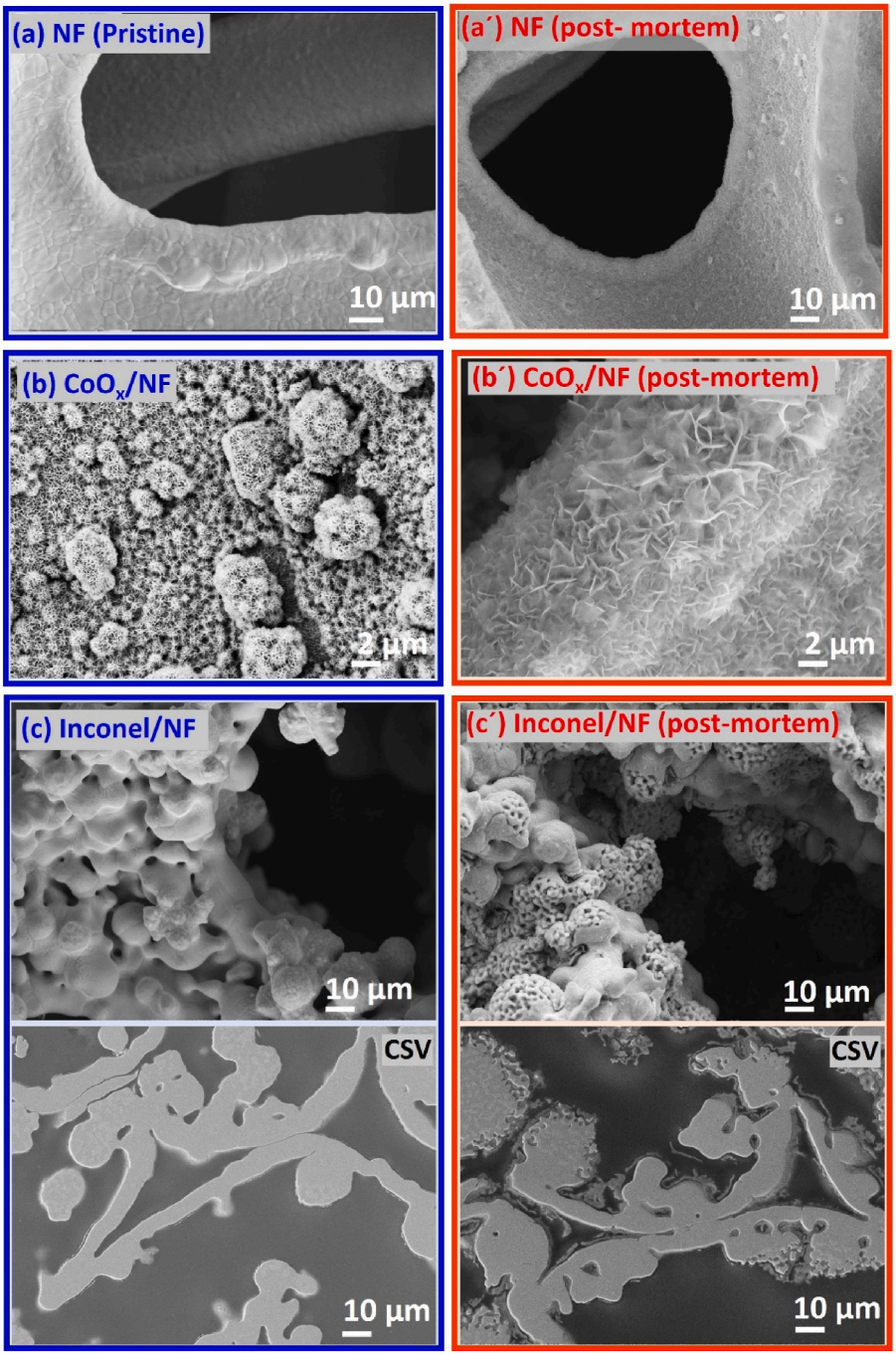

Figure 6. Electron microscopy images of (a) pristine NF, (b) CoO_x/NF, and (c) Inconel/NF electrodes prior to electrochemical testing and their corresponding images after electrochemical testing are shown in (a'), (b'), and (c'), respectively.

underwent electrochemical testing from room temperature up to 150 °C under a pressure of 45 bar in 45 wt% KOH solution. Initially, the performance of the CoO_x/NF and Inconel/NF electrodes appeared similar at 150 °C and 45 bar pressure. However, during the 108-h long-term stability test under these conditions, the CoO_x/NF electrode remained stable, requiring an overpotential of approximately 185 mV at 500 mA cm^{-2}. In contrast, the overpotential of the Inconel/NF electrode increased from 182 mV to 208 mV after 84 h of operation under the same conditions. Post-mortem investigation revealed that the microstructure of the CoO_x/NF electrode changed from an uneven macroporous Co layer to uniformly distributed nanoflakes of Ni-doped CoOOH, CoO, and Co_3O_4. The microstructure of the Inconel coating was less affected, but the Inconel particles were substantially corroded, with most of the Cr, Mo, and Nb leaching out. The pristine NF was partly oxidized to NiO, NiOOH, and Ni_2O_3. In the case of CoO_x/NF, only NiO and NiOOH were observed, likely because of the suppressed overpotential required. Overall, the CoO_x/NF electrode demonstrated remarkable electrochemical performance and stability under high temperature and pressure conditions and is a promising candidate as an HTP-AE anode.

CRediT authorship contribution statement

Pradipkumar Leuaa: Writing – review & editing, Writing – original draft, Visualization, Methodology, Formal analysis, Data curation, Conceptualization. **Yousef Alizad Farzin:** Writing – review & editing, Formal analysis, Data curation. **Sarmad Iqbal:** Writing – review &

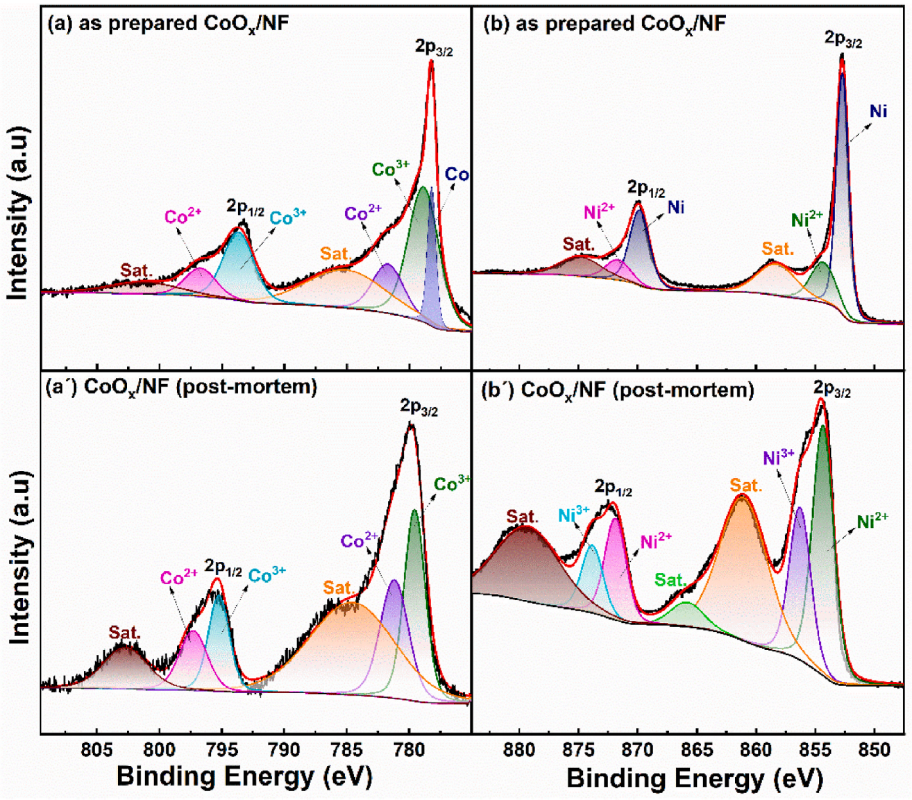

Fig. 7. (a) Co 2p and (b) Ni 2p core level XPS spectra of as prepared CoOx/NF, and (a') Co 2p and (b') Ni 2p core level XPS spectra of electrochemically tested CoO_x/NF samples.

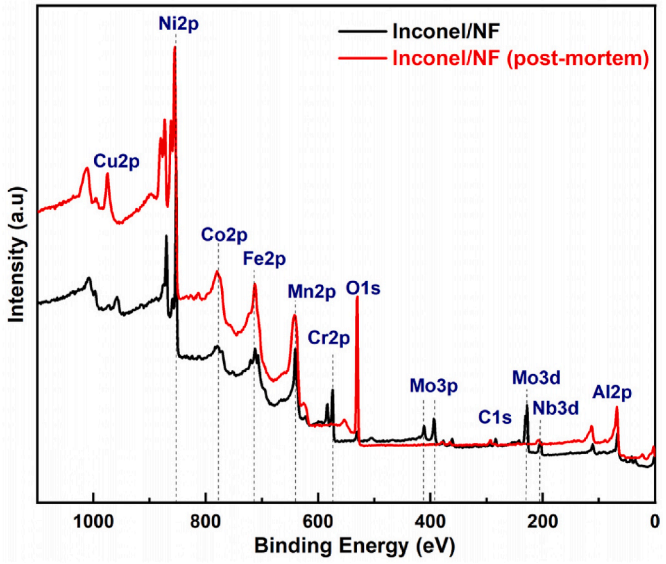

Figure 8. XPS survey spectra of pristine and electrochemically tested Inconel/NF samples.

editing, Formal analysis, Data curation. **Christodoulos Chatzichristodoulou:** Writing – review & editing, Writing – original draft, Supervision, Resources, Project administration, Funding acquisition, Conceptualization.

Declaration of competing interest

The authors declare that they have no known competing financial interests or personal relationships that could have appeared to influence the work reported in this paper.

Acknowledgements

The authors would like to acknowledge the projects *Economic and Efficient Electrolytic Hydrogen Production (EEEHy)*, funded by the Innovation Fund Denmark (grant agreement No 7046-00016B), and *Boosting Economic Electrolyzer Stack Technology 2 (BEEST2)*, funded by the EUDP program in Denmark (grant agreement No 64021-2074), for their financial support.

Appendix A. Supplementary data

Supplementary data to this article can be found online at https://doi.org/10.1016/j.jpowsour.2024.235625.

Data availability

Data will be made available on request.

References

[1] A. Raveendran, M. Chandran, R. Dhanusuraman, A comprehensive review on the electrochemical parameters and recent material development of electrochemical water splitting electrocatalysts, RSC Adv. 13 (2023) 3843–3876.
[2] C.K. Kjartansdóttir, L.P. Nielsen, P. Møller, Development of durable and efficient electrodes for large-scale alkaline water electrolysis, Int. J. Hydrogen Energy 38 (2013) 8221–8231.
[3] M. Schalenbach, O. Kasian, K.J.J. Mayrhofer, An alkaline water electrolyzer with nickel electrodes enables efficient high current density operation, Int. J. Hydrogen Energy 43 (2018) 11932–11938.
[4] K. Zeng, D. Zhang, Recent progress in alkaline water electrolysis for hydrogen production and applications, Prog. Energy Combust. Sci. 36 (2010) 307–326.

[5] F. Allebrod, C. Chatzichristodoulou, M.B. Mogensen, Alkaline electrolysis cell at high temperature and pressure of 250 °c and 42 bar, J. Power Sources 229 (2013) 22–31.

[6] F. Allebrod, C. Chatzichristodoulou, M.B. Mogensen, Cobalt and molybdenum activated electrodes in foam based alkaline electrolysis cells at 150-250 C and 40 bar, J. Power Sources 255 (2014) 394–403.

[7] F. Allebrod, C. Chatzichristodoulou, P.L. Mollerup, M.B. Mogensen, Electrical conductivity measurements of aqueous and immobilized potassium hydroxide, Int. J. Hydrogen Energy 37 (2012) 16505–16514.

[8] J.T.S. Irvine, D. Neagu, M.C. Verbraeken, C. Chatzichristodoulou, C. Graves, M. B. Mogensen, Evolution of the electrochemical interface in high-temperature fuel cells and electrolysers, Nat. Energy 1 (2016).

[9] C. Chatzichristodoulou, F. Allebrod, M.B. Mogensen, High temperature alkaline electrolysis cells with metal foam based gas diffusion electrodes, J. Electrochem. Soc. 163 (2016) F3036–F3040.

[10] P. Leuaa, D. Priyadarshani, A.K. Tripathi, M. Neergat, Internal and external transport of redox species across the porous thin-film electrode/electrolyte interface, J. Phys. Chem. C 123 (2019) 21440–21447.

[11] P. Leuaa, D. Priyadarshani, A.K. Tripathi, M. Neergat, What decides the kinetics of V2+/V3+ and VO2+/VO2+ redox reactions – surface functional groups or roughness? J. Electroanal. Chem. 878 (2020) 114590–114597.

[12] P. Leuaa, D. Priyadarshani, D. Choudhury, R. Maurya, M. Neergat, Resolving charge-transfer and mass-transfer processes of VO2+/VO2+redox species across the electrode/electrolyte interface using electrochemical impedance spectroscopy for vanadium redox flow battery, RSC Adv. 10 (2020) 30887–30895.

[13] P. Leuaa, M.R. Kraglund, C. Chatzichristodoulou, Decoupling of reaction overpotentials and ionic transport losses within 3D porous electrodes in zero-gap alkaline electrolysis cells, Electrochim. Acta 470 (2023) 143306–143314.

[14] F.P. Lohmann-Richters, S. Renz, W. Lehnert, M. Müller, M. Carmo, Review—challenges and opportunities for increased current density in alkaline electrolysis by increasing the operating temperature, J. Electrochem. Soc. 168 (2021) 114501.

[15] M. Salmanion, M.M. Najafpour, Oxygen-evolution reaction performance of nickel (Hydr)Oxide in alkaline media: iron and nickel impurities, J. Phys. Chem. C 127 (2023) 18340–18349.

[16] E. Cossar, A.O. Barnett, F. Seland, E.A. Baranova, The performance of nickel and nickel-iron catalysts evaluated as anodes in anion exchange membrane water electrolysis, Catalysts 9 (2019) 814.

[17] T. Shinagawa, M.T.K. Ng, K. Takanabe, Boosting the performance of the nickel anode in the oxygen evolution reaction by simple electrochemical activation, Angewandte Chemie - International Edition 56 (2017) 5061–5065.

[18] J. Dwlsek, P. Maunowski, J. Mergel, A.H. Schmitz, Improved components for advanced alkaline water electrolysis, Int. J. Hydrogen Energy 13 (1988) 141–511.

[19] J. Divisek, J. Mergel, H. Schmitz, Improvements of water electrolysis in alkaline media at intermediate temperatures, Int. J. Hydrogen Energy 7 (1982) 695–701.

[20] M. Prigent, T. Nenner, L. Martin, M. Roux, Hydrogen as an energy carrier, in: Proceedings of the 3rd International Seminar, Lyon, France, 1983, pp. 256–266.

[21] M. Prigent, T. Nenner, Hydrogen energy progress IV, in: Proceedings of the 4th World Hydrogen Energy Conference, Pergamon, Oxford: Pasadena, California, 1982, p. 299.

[22] M. Etzi Coller Pascuzzi, A.J.W. Man, A. Goryachev, J.P. Hofmann, E.J.M. Hensen, Investigation of the stability of NiFe-(oxy)hydroxide anodes in alkaline water electrolysis under industrially relevant conditions, Catal. Sci. Technol. 10 (2020) 5593–5601.

[23] A.J. Esswein, M.J. Mcmurdo, P.N. Ross, A.T. Bell, T.D. Tilley, Size-dependent activity of Co3O4 nanoparticle anodes for alkaline water electrolysis, J. Phys. Chem. C 113 (2009) 15068–15072.

[24] A. Pozio, F. Bozza, N. Lisi, F. Mura, Electrophoretic deposition of cobalt oxide anodes for alkaline membrane water electrolyzer, Int. J. Energy Res. 46 (2022) 952–963.

[25] D. Chanda, J. Hnát, T. Bystron, M. Paidar, K. Bouzek, Optimization of synthesis of the nickel-cobalt oxide based anode electrocatalyst and of the related membrane-electrode assembly for alkaline water electrolysis, J. Power Sources 347 (2017) 247–258.

[26] M. Hamdani, M.I.S. Pereira, J. Douch, A. Ait Addi, Y. Berghoute, M.H. Mendonça, Physicochemical and electrocatalytic properties of Li-Co3O4 anodes prepared by chemical spray pyrolysis for application in alkaline water electrolysis, Electrochim. Acta 49 (2004) 1555–1563.

[27] W.A. Badawy, F.M. Al-Kharafi, J.R. Al-Ajmi, Electrochemical behaviour of cobalt in aqueous solutions of different pH, J. Appl. Electrochem. 30 (2000) 693–704.

[28] J. Mei, T. Liao, G.A. Ayoko, J. Bell, Z. Sun, Cobalt oxide-based nanoarchitectures for electrochemical energy applications, Prog. Mater. Sci. 103 (2019) 596–677.

[29] E.M. Garcia, J.S. Santos, E.C. Pereira, M.B.J.G. Freitas, Electrodeposition of cobalt from spent Li-ion battery cathodes by the electrochemistry quartz crystal microbalance technique, J. Power Sources 185 (2008) 549–553.

[30] H. Wendt, H. Hofmann, V. Plzak, Materials research and development of electrocatalysts for alkaline water electrolysis, Mater. Chem. Phys. 22 (1989) 21–49.

[31] J. Fischer, H. Hofmann, G. Luft, H. Wendt, Fundamental investigations and electrochemical engineering aspects concerning an advanced concept for alkaline water electrolysis, AIChE J. 26 (1980) 794–802.

[32] D.Y. Chung, P.P. Lopes, P. Farinazzo Bergamo Dias Martins, H. He, T. Kawaguchi, P. Zapol, H. You, D. Tripkovic, D. Strmcnik, Y. Zhu, S. Seifert, S. Lee, V. R. Stamenkovic, N.M. Markovic, Dynamic stability of active sites in hydr(oxy) oxides for the oxygen evolution reaction, Nat. Energy 5 (2020) 222–230.

[33] Q. Zhang, W. Xiao, H.C. Fu, X.L. Li, J.L. Lei, H.Q. Luo, N.B. Li, Unraveling the mechanism of self-repair of NiFe-based electrocatalysts by dynamic exchange of iron during the oxygen evolution reaction, ACS Catal. 13 (2023) 14975–14986.

[34] H. Wang, K.H.L. Zhang, J.P. Hofmann, V.A. de la Peña O'Shea, F.E. Oropeza, The electronic structure of transition metal oxides for oxygen evolution reaction, J Mater Chem A Mater 9 (2021) 19465–19488.

[35] P. Zhai, C. Wang, Y. Zhao, Y. Zhang, J. Gao, L. Sun, J. Hou, Regulating electronic states of nitride/hydroxide to accelerate kinetics for oxygen evolution at large current density, Nat. Commun. 14 (2023) 1873.

[36] J. Chen, G. Zhao, Y. Chen, K. Rui, H. Mao, S.X. Dou, W. Sun, Iron-doped nickel molybdate with enhanced oxygen evolution kinetics, Chem. Eur J. 25 (2019) 280–284.

[37] R. Fu, C. Feng, Q. Jiao, K. Ma, S. Ge, Y. Zhao, Molybdate intercalated nickel–iron-layered double hydroxide derived Mo-doped nickel–iron phosphide nanoflowers for efficient oxygen evolution reaction, Energy Materials and Devices 1 (2023) 9370002.

[38] M. Zhang, X. He, K. Dong, H. Zhang, Y. Yao, C. Yang, M. Yue, S. Sun, Y. Sun, D. Zheng, Y. Luo, Q. Liu, N. Li, B. Tang, J. Liu, X. Sun, Chromium doping enabled improvement in alkaline seawater oxidation over cobalt carbonate hydroxide nanowire array, Chem. Commun. 59 (2023) 9750–9753.

[39] Y. Lin, Z. Tian, L. Zhang, J. Ma, Z. Jiang, B.J. Deibert, R. Ge, L. Chen, Chromium-ruthenium oxide solid solution electrocatalyst for highly efficient oxygen evolution reaction in acidic media, Nat. Commun. 10 (2019).

[40] C.C. Lin, C.C.L. McCrory, Effect of chromium doping on electrochemical water oxidation activity by Co3-xCrxO4 spinel catalysts, ACS Catal. 7 (2017) 443–451.

[41] J. Zhao, X. Liu, X. Ren, B. Du, X. Kuang, D. Tian, Q. Wei, D. Wu, Chromium doping: a new approach to regulate electronic structure of cobalt carbonate hydroxide for oxygen evolution improvement, J. Colloid Interface Sci. 609 (2022) 414–422.

[42] M. Plevová, J. Hnát, K. Bouzek, Electrocatalysts for the oxygen evolution reaction in alkaline and neutral media. A comparative review, J. Power Sources 507 (2021) 230072.

[43] F. Rosalbino, S. Delsante, G. Borzone, G. Scavino, Electrocatalytic activity of crystalline Ni-Co-M (M = Cr, Mn, Cu) alloys on the oxygen evolution reaction in an alkaline environment, Int. J. Hydrogen Energy 38 (2013) 10170–10177.

[44] C. Chatzichristodoulou, F. Allebrod, M. Mogensen, High temperature and pressure electrochemical test station, Rev. Sci. Instrum. 84 (2013) 054101.

[45] P. Leuaa, C. Chatzichristodoulou, Reversible hydrogen and Pd hydride reference electrodes with electrochemically supplied H 2 for high temperature and pressure electrochemistry, J. Electrochem. Soc. 169 (2022) 054534.

[46] S. Liu, L. Zhao, B. Cui, X. Liu, W. Han, J. Zhang, W. Xiang, A long life and high efficient rechargeable hybrid zinc-air/Co3O4 battery with stable high working voltage, Ionics 26 (2020) 767–775.

[47] L.J. Garces, B. Hincapie, R. Zerger, S.L. Suib, The effect of temperature and support on the reduction of cobalt oxide: an in situ x-ray diffraction study, J. Phys. Chem. C 119 (2015) 5484–5490.

[48] B. Lu, D. Cao, P. Wang, G. Wang, Y. Gao, Oxygen evolution reaction on Ni-substituted Co3O4 nanowire array electrodes, Int. J. Hydrogen Energy 36 (2011) 72–78.

[49] R.C. Xie, M. Volokhova, A. Boldin, L. Seinberg, M. Tsujimoto, M. Yang, B. Rasche, R.G. Compton, Electrocatalytic oxidation of hydroxide ions by Co3O4 and Co3O4@SiO2 nanoparticles both at particle ensembles and at the single particle level, Chemelectrochem 7 (2020) 1261–1276.

[50] J. Balej, Determination of the oxygen and hydrogen overvoltage in concentrated alkali hydroxide solutions, Int. J. Hydrogen Energy 10 (1985) 365–374.

[51] D.M. Guzman-Bucio, G. Gomez-Sosa, D. Cabrera-German, J.A. Torres-Ochoa, M. Bravo-Sanchez, O. Cortazar-Martinez, A.J. Carmona-Carmona, A. Herrera-Gomez, Detailed peak fitting analysis of the Ni 2p photoemission spectrum for metallic nickel and an initial oxidation, J Electron Spectros Relat Phenomena 262 (2023) 147284.

[52] P. Dubey, N. Kaurav, R.S. Devan, G.S. Okram, Y.K. Kuo, The effect of stoichiometry on the structural, thermal and electronic properties of thermally decomposed nickel oxide, RSC Adv. 8 (2018) 5882–5890.

[53] P. Salunkhe, A.V. Muhammed Ali, D. Kekuda, Investigation on tailoring physical properties of Nickel Oxide thin films grown by dc magnetron sputtering, Mater. Res. Express 7 (2020) 016427.

[54] Y. Alizad Farzin, A. Babaei, T. Løye Skafte, E. Stamate, A. Ataie, S.H. Jensen, Development of an SFMM/CGO composite electrode with stable electrochemical performance at different oxygen partial pressures, Int. J. Hydrogen Energy 47 (2022) 7915–7931.

[55] Y. Alizad Farzin, M. Bjerg Mogensen, S. Pirou, H. Lund Frandsen, Perovskite/Ruddlesden-Popper composite fuel electrode of strontium-praseodymium-manganese oxide for solid oxide cells: an alternative candidate, J. Power Sources 580 (2023) 233450.

[56] M.C. Biesinger, B.P. Payne, A.P. Grosvenor, L.W.M. Lau, A.R. Gerson, R.S.C. Smart, Resolving surface chemical states in XPS analysis of first row transition metals, oxides and hydroxides: Cr, Mn, Fe, Co and Ni, Appl. Surf. Sci. 257 (2011) 2717–2730.

[57] C. Belkessam, S. Bencherif, M. Mechouet, N. Idiri, J. Ghilane, The effect of heteroatom doping on nickel cobalt oxide electrocatalysts for oxygen evolution and reduction reactions, Chempluschem 85 (2020) 1710–1718.

[58] A.P. Grosvenor, M.C. Biesinger, R.S.C. Smart, N.S. McIntyre, New interpretations of XPS spectra of nickel metal and oxides, Surf. Sci. 600 (2006) 1771–1779.

[59] D. Rodriguez, A. Merwin, Z. Karmiol, D. Chidambaram, Surface chemistry and corrosion behavior of Inconel 625 and 718 in subcritical, supercritical, and ultrasupercritical water, Appl. Surf. Sci. 404 (2017) 443–451.